Robotics and Computer-Integrated Manufacturing 39 (2016) 22–31

Contents lists available at ScienceDirect

Robotics and Computer-Integrated Manufacturing

journal homepage: www.elsevier.com/locate/rcim

Full length Article

Impact & improvement of tool deviation in friction stir welding: Weld quality & real-time compensation on an industrial robot ☆

Mario Guillo *, Laurent Dubourg

Institut Maupertuis, Contour Antoine de St-Exupéry Campus de Ker Lann, 35170 Bruz, France

ARTICLE INFO

Article history:
Received 6 June 2015
Received in revised form
24 October 2015
Accepted 6 November 2015

Keywords:
Robotic Friction Stir Welding
Industrial robot
Welding process
Robot deviation
Weld quality
Path compensation

ABSTRACT

The present study proposes the use of an industrial serial robot to reduce the investment cost and to increase the process flexibility of Friction Stir Welding (FSW). The first part of the study characterizes the impact of pin axis position on FS Weld (FSWed) quality. The second part shows a method to compensate the lateral pin deviation in real-time during Robotic Friction Stir Welding (RFSW). This paper shows that a robot with an embedded real-time algorithm for the compensation of the lateral tool deviation can reproduce the same FSWed quality as a gantry-type CNC system. The elastostatic model of an industrial robot is carried out by the classical identification technique and this is embedded in the robot controller. Based on force measurements along the welding process, the corrected path is calculated in real-time.

© 2015 Elsevier Ltd. All rights reserved.

1. Introduction

FSW is an emerging manufacturing technology for aerospace, automotive, railway and civil structures. It offers ways of designing lighter structures at lower manufacturing cost than traditional joining methods: fusion welding, riveting or adhesive bonding [1,2]. As illustrated in Fig. 1, FSW process involves a rotating tool consisting of a pin and a shoulder.

The pin is inserted between adjoining metal pieces and the shoulder is placed at the top surface of the joint. The heat generated by the tool friction brings the metal to a viscoplastic state, while the pin stirs the two pieces together. Severe plastic deformation, and flow of this plasticised metal occurs as the tool is translated along the welding direction. Material is transported from the front of the pin to the trailing edge where it is forged into a sound and homogenous joint. Since the invention of FSW in 1991 by The Welding Institute (TWI), many studies have demonstrated its capability for joining a wide range of materials. Unlike fusion welding, the melting point of the welded materials is not reached during FSW. This reduces the probability of distortion, porosity and loss of mechanical properties of weldments. Moreover, the technology can be applied to hot cracking sensitive aluminium alloys, such as 2xxx [3,4] and 7xxx series [5], which are considered to be difficult to weld by using traditional processes. However, the FSW manufacturing parameters impact significantly the weld quality. Therefore, the tool weld speed, the rotationnal speed [6–8] and the pin position in the weldment [9] have to be carefully selected and controlled. These welding parameters have important effects on material properties, such as the metallurgical microstructure, defects (porosity, lack of penetration), hardness, electric conductivity and tensile strength. Currently, gantry-type CNC systems are being used for FSW manufacturing. These machines offer a high stiffness and can tolerate the high forces during FSW in order to produce a good weld quality. For 10 years [10–14] an effort is done to replace dedicated gantry-type machines with industrial serial robots to reduce the investment cost and to increase the process flexibility. However, two limitations of RFSW can be highlighted. The first one is the payload capability of industrial robots which limits the welding thickness up to 8 mm for aluminium materials (AW-5083-H111, AW-6060-T66, AC-46000) [15]. The second limitation is the low stiffness of the robotic joints and, thus, the important elasticity of serial robots [16–19]. Consequently, the robot deformations under the high process forces cause both axial and lateral FSW tool deviations (about several millimeters) [20,21], impacting the weld quality. Axial tool

☆This work is part of a larger project named: "Study of industrial robot behavior under static and dynamic loads during Friction Stir Welding and finding of improvement solutions". This project is co-financed by the European Union and Brittany region and done in collaboration with E. Ragneau, E. Courteille, P. Maurine (INSA Rennes-LGCGM). The European Union invests in Brittany through the European Regional Development Fund.

* Corresponding author.
E-mail addresses: mario.guillo@institutmaupertuis.fr (M. Guillo), laurent.dubourg@institutmaupertuis.fr (L. Dubourg).

http://dx.doi.org/10.1016/j.rcim.2015.11.001
0736-5845/© 2015 Elsevier Ltd. All rights reserved.

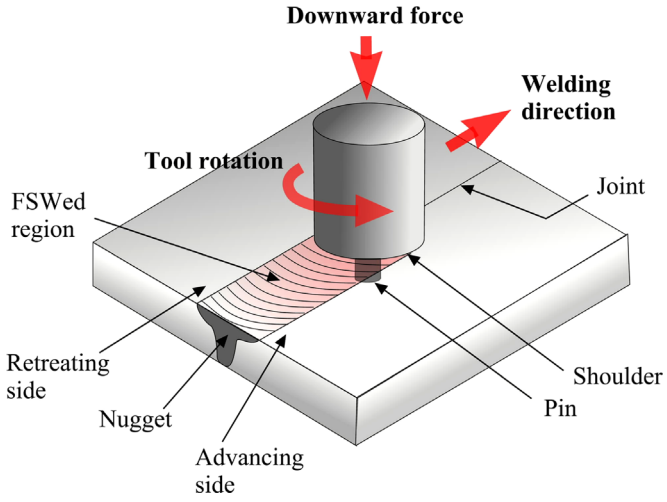

Fig. 1. Description of the FSW process.

deviation is currently compensated by the well-documented force control approach [22,13,23]. However, for butt joint configuration, the lateral deviation can modify the position of pin axis and cause lack-of-penetration defects reducing significantly the mechanical resistance of FSW weldments [9]. In RFSW, the lateral deviation is not measured by the robot joint encoders and is uncontrolled as it depends on the process loads and robot configurations [24]. The first part of the paper characterizes the impact of pin axis position on FSWed quality, especially on the appearance of lack-of-penetration defect, and on the tensile strength properties. This experiment is carried out on a gantry-type CNC system in order to use a high stiffness machine and to control accurately the pin position. The second part shows a method to compensate the lateral deviation in real-time during RFSW and the associated improvements on the weld quality. A real-time algorithm embedded in the industrial robot controller calculates the lateral deviation based on the FSW force measurements and the knowledge of the elastic robot structure.

2. Experimental set up

FSW of AA 5754-H22 sheets is performed using coupons of 300-mm long by 100-mm wide by 3 mm thick in butt configuration as shown in Fig. 2. The rolling direction of the coupons is placed parallel to the welding path. Samples are positioned on a steel backing anvil and clamped along the two long edges.

FSW trials are carried out on a Vernier CNC system in the first part of the study as shown in Fig. 3. In the second part of the study, RFSW experiments are performed on a test-bed incorporating a FANUC S900iB/400 RJ3iB industrial robot and an electrically driven process end-effector as shown in Fig. 4. The payload capability of this robot is 400 kg, with a maximum reach of 2488 mm and a repeatability of $\pm$ 0.5 mm.

As shown in Fig. 5, weldments are produced with a FSW tool made of H13 tool steel and composed of a pin and a shoulder. The pin is a conical left-hand threaded pin of 3-mm diameter and 2.8-mm long. The shoulder is a scroll shape with a diameter of 8.5 mm.

The welding parameters consist in a rotational speed of 1200 RPM, a traveling speed of 6 mm/s and a tilt angle of 0° as illustrated in Fig. 6. During the trials on the CNC system, position control welding mode is used with a fixed shoulder penetration of 0.1-mm depth. For RFSW experiments, force control welding mode is activated to produce samples (a vertical forge force of 3.1 kN). In FSW mass production, the force control mode results in more repeatable weld quality than position control welding mode [23]. In the present study, this mode is used to compensate the axial tool deviation along the normal sample axis due to the robot

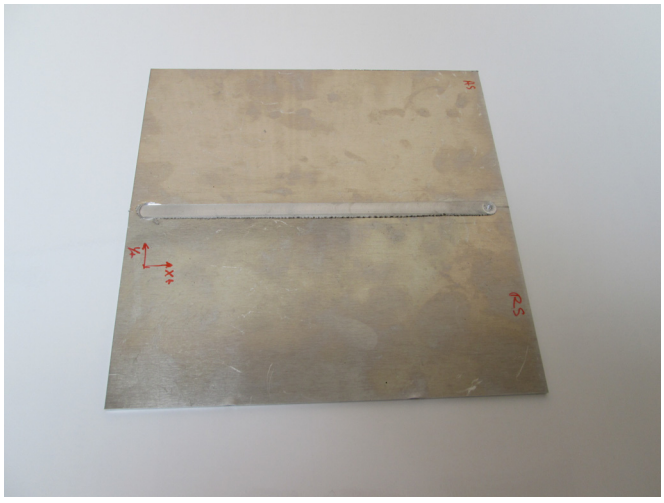

Fig. 2. 3-mm thick AA 5754-H22 FSWed coupons.

Fig. 3. Gantry type Vernier CNC machine.

Fig. 4. RFSW test-bed incorporating a FANUC S900iB/400 RJ3iB industrial robot and an electrically driven process end-effector.

deformation. The force control during RFSW is documented by several authors [22,13,25]. In order to characterize the impact of pin position on FSWed quality, the first experiments are carried out on a gantry-type CNC system. The CNC system architecture offers a high stiffness to control accurately the pin position. The position of the pin axis is measured from the weld seam as schematically shown in Fig. 6. The pin offset is ranging from −1.5 to 1.5 mm in direction of the advancing side of the FSW tool.

The second part shows a method to compensate the lateral deviation in real-time during RFSW and the improvement of the associated weld quality. A real-time algorithm embedded in the industrial robot controller calculates the lateral deviation based on the FSW force measurements and the knowledge of the elastic robot structure [26–28].

For microstructure observation, the cross section of the welds is polished to a mirror like finish (diamond paste with a grain size of 0.5 μm) and etched with Keller's reagent. For bending and tensile characterisation, 25-mm wide coupons are machined out from the welded panel and perpendicular to the welding direction. Bending tests are manually performed according to ISO 5173:2009 standard (Destructive tests on welds in metallic materials – Bend tests). This is done solely to characterize the weld quality and to determine the fracture location. No attempt is made to measure the force. The failed coupons are examined using optical microscopy. For each welding condition, three sub-size tensile coupons are prepared according to ISO 4136:2001 standard (Destructive tests on welds in metallic materials – Transverse tensile test). Cross sections of 25-mm width and 50-mm gauge length are used for all-welded samples.

Fig. 5. FSW tool used for experiments.

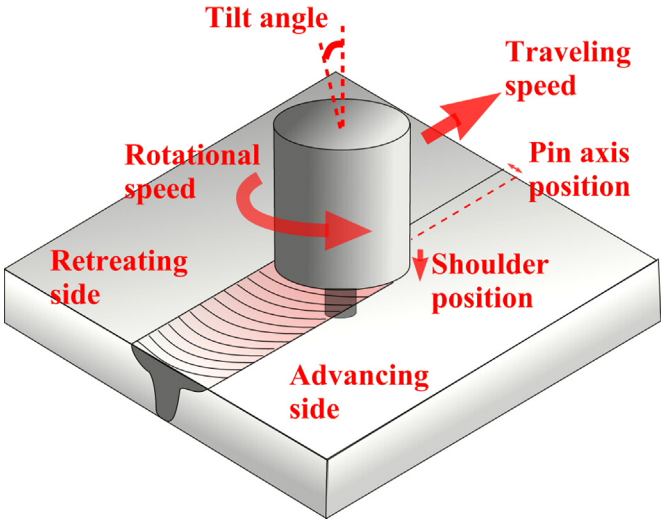

Fig. 6. FSW parameters in this work.

3. Results and discussion

3.1. FSW trials on CNC system

Fig. 7 shows cross sections of welds with pin offsets from −1.5 mm to 1.25 mm. Metallographic examinations with a high magnification reveal the presence of lack of penetration and kissing-bond defects with pin positions of −1.5 and 1.25 mm. The kissing bond defect consists in a thin layer of oxide located at the intimate contact of two adjacent surfaces without actual metallurgical bond and lack of cohesion forces [29]. This type of defect propagates from the tip of the lack of penetration and along the weld nugget boundary. These types of flaws are very common in FSWed butt-joints and are generally due to an excessive distance between the pin and the backing anvil [30]. The vertical force applied on the welding tool facilitates a correct pin penetration, but the contact with the backing surface could damage the tool and the welding setup. In general, the pin-to-back distance is always larger than zero [30]. In our experiments, a lack of penetration and kissing-bond defects occur when the pin position is placed away from the weld seam (pin offsets lower than −1.5 mm or higher than 1.25 mm). Here, the sample edges are not completely stirred in the weld root by the pin rotation. However, this phenomenon is not symmetrical according to the weld seam, the advancing side of the FSW tool handling a slightly higher pin offset. This dissymmetry could be explained by the higher strain rate in the advancing side of the weld.

The lack of penetration defect is not perpendicular to the surface of the coupon, as it shows an oblique orientation, making an angle with the surface normal (vertical) starting at about 200° and it increases as the tool depth progresses, reaching a value of 59° at 150 mm from the weld bottom. This orientation of the defects is expected due to the stirring of the plasticized metal and to the geometry of the pin.

Fig. 8 shows the results of the bending tests at the same discrete locations at which the metallurgical cross sections are presented. The overall observation is that the bending causes the specimen to break when the lack of penetration defect is present, i.e. pin offsets lower than −1.5 mm (Fig. 7b) or higher than 1.25 mm (Fig. 7d). For pin positions between −1.25 and 1 mm, no failure is observed by optical microscopy as shown in Fig. 7c.

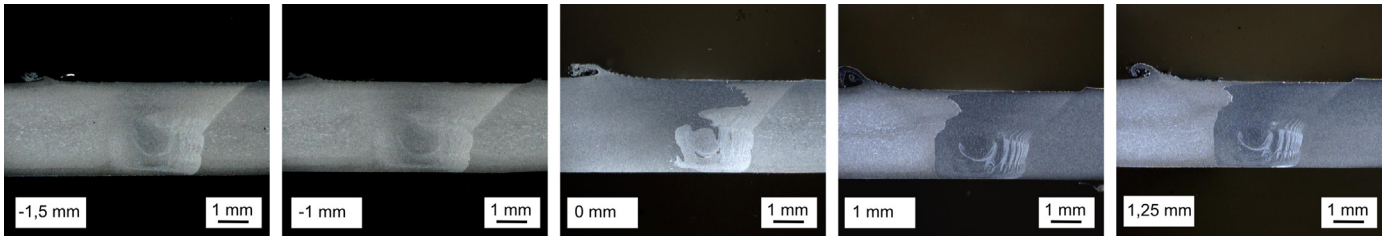

Fig. 7. Metallurgical cross sections of welds with pin positions from −1.5 mm to 1.25 mm

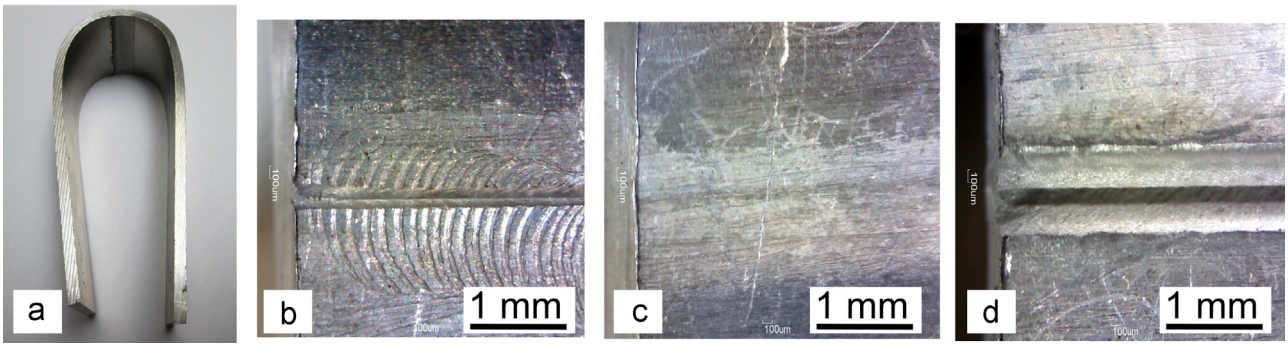

Fig. 8. (a) Example of bending test, (b) bending test results with pin positions of (b) −1.5 mm, (c) 0 mm and (d) 1.25 mm

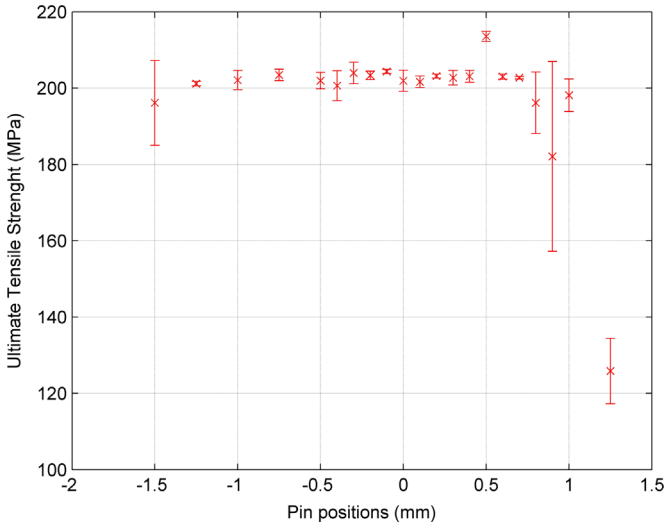

Fig. 9. UTS of FSWed coupons as a function of pin positions.

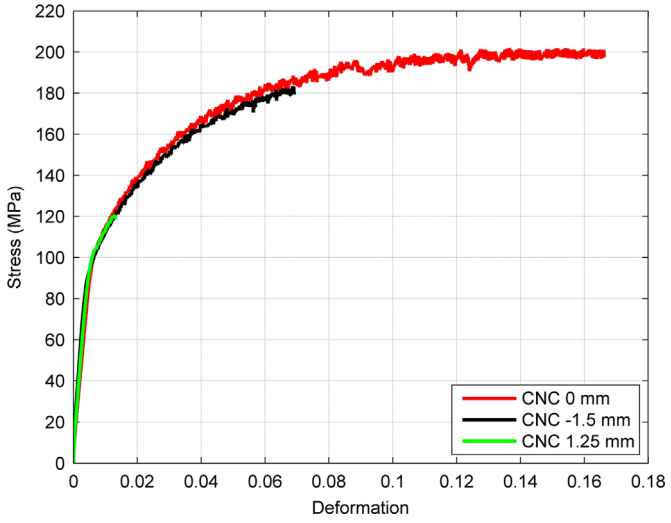

Fig. 10. Stress-strain curves of FSWed coupons with pion offsets of −1.5, 0 and 1.25 mm

The Ultimate Tensile Strength (UTS) of FSWed coupons are shown as a function of pin positions in Fig. 9. For pin positions between −1.25 and 0.7 mm, UTS ranges between 201 and 214 MPa and is not impacted by the pin offset. As compared with the base material, the joint efficiency is about 100%. This high weld quality is confirmed by the tensile failure occurring in the base metal. For welding conditions with pin positions lower than −1.25 mm and higher than 0.7 mm, UTS decreases and the failure occurs in the weld nugget. The corresponding welded specimens present a lower ductility than the base material as shown in Fig. 10. The UTS and the ductility reduction confirm the presence of a weld defect due to an excessive pin position offset. As bending test results, the defect occurrence is not symmetrical according to the weld seam. As mentioned previously, the dissymmetry phenomenon could be explained by the higher strain rate in the advancing side of FSWed.

FSW trials on CNC system and the associated characterizations show that the pin could be located into an offset of about −1.25 and 0.7 mm around the seam without impacting the weld quality. This result is obtained with a pin diameter of 3 mm. These observations are in accordance with Dubourg et al. [9] in two set-ups, an offset of the pin position up to 0.8 mm for 2-mm thick AA7075-T6 welding (pin diameter of 3 mm) and 3-mm for 8-mm thick AA6061-T6 welding (pin diameter of 8 mm) does not significantly affect UTS.

3.2. RFSW experiments on industrial robot

3.2.1. DH parameters of the FANUC S900iB/400 robot

The kinematic of the FANUC S900iB/400 robot closed-loop chain is shown in Fig. 11. The modified Denavit Hartenberg (DH) notation is used [31]. As illustrated in Fig. 11, the robot has $L=9$ revolute joints ($\theta_j = q_j$), $n+1=9$ links and $N=6$ active joints, where C_0 is the fixed base and $B = L - n = 1$ closed-loop. The geometric description of the robot structure with closed-loops is defined by an equivalent tree structure obtained by cutting each closed-loop at its joint and by adding two frames at each cut joint [31]. The ($L \times 1$) joint variable vector is written $\mathbf{q} = [\mathbf{q}_a\ \mathbf{q}_p\ \mathbf{q}_c]^T$ with:

- $\mathbf{q}_a$: the vector containing the $N=6$ active joint variables.
- $\mathbf{q}_p$: the vector containing the $p = n - N = 3$ passive joint variable of the equivalent tree structure.
- $\mathbf{q}_c$: the vector containing the $B=1$ variables of the cut joints.

For the FANUC S900iB/400 robot, the joint variable vector is:

$$\begin{cases} \mathbf{q}_a = [q_1\ q_2\ q_4\ q_5\ q_6\ q_7]^T \\ \mathbf{q}_p = [q_3\ q_8]^T \\ \mathbf{q}_c = q_9. \end{cases} \quad (1)$$

Moreover, the relations between $\mathbf{q}$ joint variables (constraint closed-loop equations) can be calculated by the following relation: $C = L - N = 9 - 6 = 3$. For the FANUC S900iB/400 robot, the closed-loop constraints are:

$$\begin{cases} q_3 = q_9 \\ q_9 = -q_8 \\ q_8 = -q_2 - q_7. \end{cases} \quad (2)$$

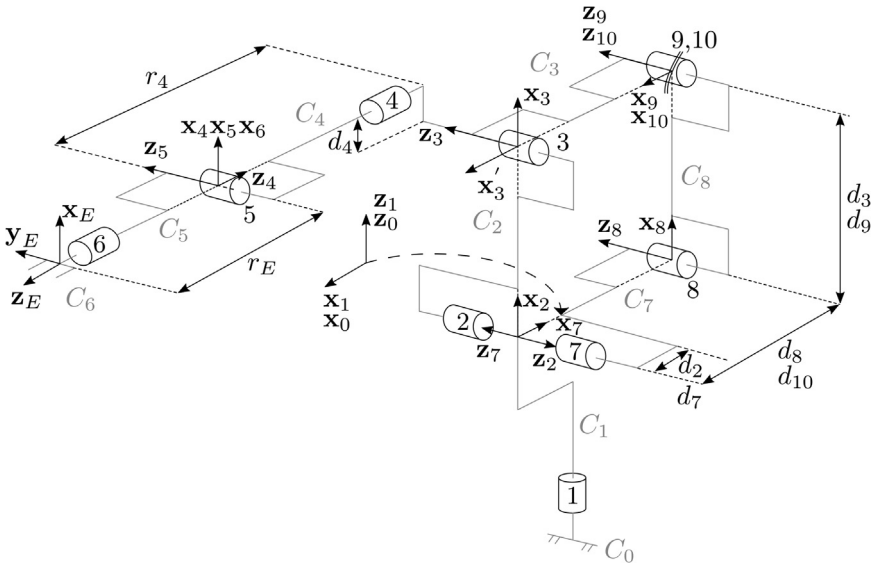

Fig. 11. Modeling of the FANUC S900iB/400 robot.

Table 1
DH parameters of the FANUC S900iB/400 robot.

j	$a(j)$	μ_j	σ_j	γ_j	b_j	α_j	d_j	θ_j	r_j
1	0	1	0	0	0	0	0	θ_1	0
2	1	1	0	0	0	$-\frac{\pi}{2}$	d_2	$-\frac{\pi}{2}+\theta_2$	0
3	2	0	0	0	0	π	d_3	θ_3	0
4	3	1	0	0	0	$-\frac{\pi}{2}$	d_4	θ_4	$-r_4$
5	4	1	0	0	0	$\frac{\pi}{2}$	0	θ_5	0
6	5	1	0	0	0	$-\frac{\pi}{2}$	0	θ_6	0
7	1	1	0	0	0	$\frac{\pi}{2}$	d_7	$\pi+\theta_7$	0
8	7	0	0	0	0	0	d_8	$-\frac{\pi}{2}+\theta_8$	0
9	8	0	0	0	0	0	d_9	$-\frac{\pi}{2}+\theta_9$	0
10	3	0	0	$-\frac{\pi}{2}$	0	0	$-d_{10}$	0	0
E	6	0	0	0	0	π	0	0	r_E

The DH parameters of the FANUC S900iB/400 robot are given in Table 1.

3.2.2. Kinematic jacobian matrix of the FANUC S900iB/400 robot

The 6 × 6 kinematic jacobian matrix $\mathbf{J}$ of the robot links the joint rates with the linear and angular velocity (twist) of the robot Tool Center Point (TCP) according to:

$$\dot{\mathbf{X}} = \begin{bmatrix} \mathbf{V} \\ \boldsymbol{\omega} \end{bmatrix} = \mathbf{J}\dot{\mathbf{q}}_m \tag{3}$$

where:

$$\begin{cases} \dot{\mathbf{q}}_m = [\dot{q}_1\ \dot{q}_2\ \dot{q}_3\ \dot{q}_4\ \dot{q}_5\ \dot{q}_6]^T \\ \dot{q}_3 = \dot{q}_2 + \dot{q}_7. \end{cases} \tag{4}$$

$\dot{\mathbf{X}}$ is the TCP twist, composed of the translational velocity vector $\mathbf{V}$ and the angular velocity vector $\boldsymbol{\omega}$.

3.2.3. Kinetostatic performance index

According to Dumas et al. [27], the optimal robot configurations for the joint stiffness identification are chosen where the robot shows a high dexterity. The robot dexterity is calculated using the Frobenius norm. The Frobenius norm is defined as follows:

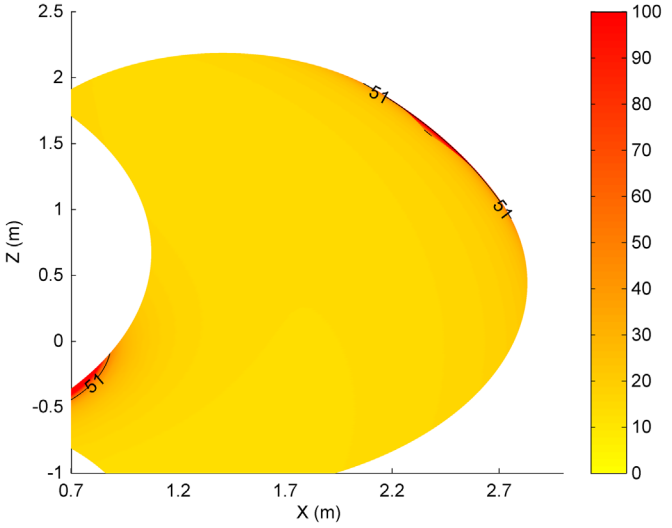

Fig. 12. $\kappa_f(\mathbf{J})$ isocontours into the robot cartesian workspace.

$$\kappa_f(\mathbf{J}) = \frac{1}{6}\sqrt{\mathrm{tr}(\mathbf{J}^T\mathbf{J})\mathrm{tr}[(\mathbf{J}^T\mathbf{J})^{-1}]} \tag{5}$$

The first joint q_1 does not affect the robot dexterity, as q_1 is null. The wrist joints q_4, q_5 and q_6 are set to 45° in order to avoid the wrist configuration singularity.

Fig. 12 depicts $\kappa_f(\mathbf{J})$ isocontours into the robot cartesian workspace. The robot dexterity increases with the decrease of the $\kappa_f(\mathbf{J})$ factor. As illustrated in Fig. 12, the robot dexterity is high into the overall cartesian workspace, showing the high quality of the mechanical design of the FANUC S900iB/400 robot. The workspace boundaries show a high $\kappa_f(\mathbf{J})$ factors and should be avoided for the joint stiffness identification.

3.2.4. Formulation of the cartesian stiffness matrix

In many industrial robots, the dominant source of the robot deformation comes from the compliance in the joints (harmonic drives and motors) [19,17]. In this paper, the following assumptions are used:

- The links of the robot are assumed to be rigid.
- The joint stiffness is represented by linear torsional springs.

Then, the cartesian matrix formulation can be defined as follows:

$$\begin{cases} \mathbf{F}_e = \mathbf{K}_X \Delta\mathbf{X} \\ \mathbf{K}_X = \mathbf{J}^{-T}(\mathbf{K}_q - \mathbf{K}_c)\mathbf{J}^{-1} \\ \mathbf{K}_q = Diag\left[k_{q1}\ k_{q2}\ k_{q3}\ k_{q4}\ k_{q5}\ k_{q6}\right] \\ \mathbf{K}_c = \left[\frac{\partial \mathbf{J}^T}{\partial q_1}\mathbf{F}_e\ \frac{\partial \mathbf{J}^T}{\partial q_2}\mathbf{F}_e\ \frac{\partial \mathbf{J}^T}{\partial q_3}\mathbf{F}_e\ \frac{\partial \mathbf{J}^T}{\partial q_4}\mathbf{F}_e\ \frac{\partial \mathbf{J}^T}{\partial q_5}\mathbf{F}_e\ \frac{\partial \mathbf{J}^T}{\partial q_6}\mathbf{F}_e\right] \end{cases} \quad (6)$$

where $\mathbf{K}_X$ is the cartesian stiffness matrix. $\mathbf{F}_e$ is the six-dimensional wrench vector composed of forces and torques applied on the robot TCP. $\Delta\mathbf{X}$ is the six-dimensional vector composed of the translational and rotational displacements of the robot TCP. $\mathbf{K}_q$ is the diagonal joint stiffness matrix and $\mathbf{K}_c$ is the complementary stiffness matrix [32].

3.2.5. Joint stiffness identification

According to Dumas et al. [27], the identification of the joint stiffness values can be simplified if the complementary stiffness matrix $\mathbf{K}_c$ is negligible compared to $\mathbf{K}_q$. In this case, Eq. (6) becomes:

$$\mathbf{K}_X \simeq \mathbf{J}^{-T}\mathbf{K}_q\mathbf{J}^{-1}. \quad (7)$$

Moreover, Eq. (7) presents a computational advantage for real-time path compensation. As shown in Eq. (6), the increase of the wrench on the robot TCP increases the influence of $\mathbf{K}_c$ on $\mathbf{K}_X$. The vector $\| \Delta\mathbf{X} \|$ of the robot TCP displacement is expressed as follows:

$$\| \Delta\mathbf{X} \| = \sqrt{\delta x^2 + \delta y^2 + \delta z^2}. \quad (8)$$

Only the translational displacements are considered in Eq. (8) due to the cartesian movements in RFSW experiments. The index ν_p characterizes the influence of $\mathbf{K}_c$ on the evaluation of the robot translational displacements. This can be expressed:

$$\nu_p = \frac{\left| \| \Delta\mathbf{X}_{\mathbf{K}_c} \| - \| \Delta\mathbf{X}_{\bar{\mathbf{K}}_c} \| \right|}{\max\left(\| \Delta\mathbf{X}_{\mathbf{K}_c} \|, \| \Delta\mathbf{X}_{\bar{\mathbf{K}}_c} \| \right)} \quad (9)$$

where $\| \Delta\mathbf{X}_{\mathbf{K}_c} \|$ is the displacement norm of the robot TCP with $\mathbf{K}_c$ calculated according to Eq. (6). $\| \Delta\mathbf{X}_{\bar{\mathbf{K}}_c} \|$ is the displacement norm of the robot TCP, assuming that $\mathbf{K}_c$ is null. $\mathbf{F}_e$ is the maximum capabilities of the FANUC S900iB/400 robot. In first estimation, $\mathbf{K}_q$ is chosen according to values in Dumas et al. [27]. $\mathbf{F}_e$ (N and Nm) and $\mathbf{K}_q$ (Nm/rad) are defined as follows:

$$\begin{cases} \mathbf{F}_e = \left[1000\ \ -3000\ \ -4000\ \ -200\ 200\ \ -200\right]^T \\ \mathbf{K}_q = Diag\left[1.\ 10^6\ 4.\ 10^5\ 4.\ 10^5\ 1.\ 10^4\ 1.\ 10^4\ 1.\ 10^4\right]. \end{cases} \quad (10)$$

Fig. 13 illustrates the ν_p isocontours into the robot cartesian workspace. When the ν_p value increases, the impact of $\mathbf{K}_c$ on the evaluation of the robot TCP displacements increases too.

As shown in Fig. 13, ν_p value is very small ($\nu_p \leq 0.03$). Consequently, we can assume that Eq. (7) is valid in the overall robot cartesian workspace. The six-dimensional robot TCP displacement vector $\Delta\mathbf{X}$ is expressed as follows:

$$\Delta\mathbf{X} = \left(\mathbf{J}\mathbf{K}_q^{-1}\mathbf{J}^T\right)\mathbf{F}_e. \quad (11)$$

The six-dimensional compliance vector $\mathbf{c}$ is defined:

$$\mathbf{c} = \left[\frac{1}{k_{q1}}\ \frac{1}{k_{q2}}\ \frac{1}{k_{q3}}\ \frac{1}{k_{q4}}\ \frac{1}{k_{q5}}\ \frac{1}{k_{q6}}\right]^T. \quad (12)$$

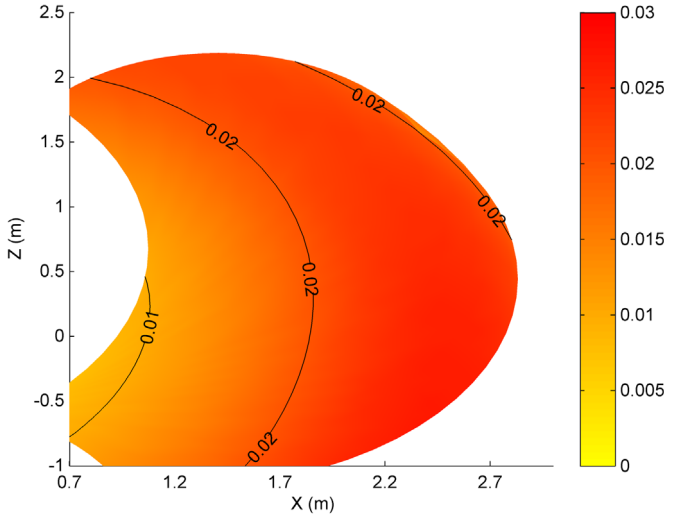

Fig. 13. ν_p isocontours into the robot cartesian workspace.

Table 2
Joint stiffness values (Nm/rad) of the FANUC S900iB/400 robot.

k_{q1}	k_{q2}	k_{q3}	k_{q4}	k_{q5}	k_{q6}
5.73. 10^6	5.37. 10^6	1.49. 10^6	5.8. 10^4	8.5. 10^4	5.8. 10^4

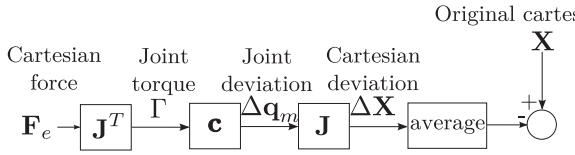

Fig. 14. Block diagram of the real time compensation.

Eq. (11) can be expressed as follows:

$$\mathbf{W}\mathbf{c} = \Delta\mathbf{X} \quad (13)$$

where $\mathbf{W}$ is 6 $\times$ 6 matrix as follows:

$$\mathbf{W} = \begin{bmatrix} J_{11}\sum_{i=1}^{6} J_{i1}F_i & \cdots & \cdots & \cdots & \cdots & J_{16}\sum_{i=1}^{6} J_{i6}F_i \\ \cdots & & \cdots & & & \cdots \\ \cdots & & \cdots & & & \cdots \\ \cdots & & \cdots & & & \cdots \\ \cdots & & \cdots & & & \cdots \\ J_{61}\sum_{i=1}^{6} J_{i1}F_i & \cdots & \cdots & \cdots & \cdots & J_{66}\sum_{i=1}^{6} J_{i6}F_i \end{bmatrix}. \quad (14)$$

As a consequence, for $n > 1$ measurements, the matrix $\mathbf{W}$ becomes $6n \times 6$ and the resolution of Eq. (13) is an overdetermined problem. This can be resolved by Ordinary Least Squares (OLS) method. The $\mathbf{c}$ value that minimizes the OLS problem is:

$$\mathbf{c} = \left(\mathbf{W}^T\mathbf{W}\right)^{-1}\mathbf{W}^T\Delta\mathbf{X} = \mathbf{W}'\Delta\mathbf{X} \quad (15)$$

where $\mathbf{W}'$ is the generalized inverse (pseudoinverse) of $\mathbf{W}$. According to the previous sections, 20 measurements are chosen into the FANUC S900iB/400 robot cartesian workspace. The used identification technique is well-documented in the literature [27,26,28]. The identified joint stiffness values measuring on the FANUC S900iB/400 are shown in Table 2.

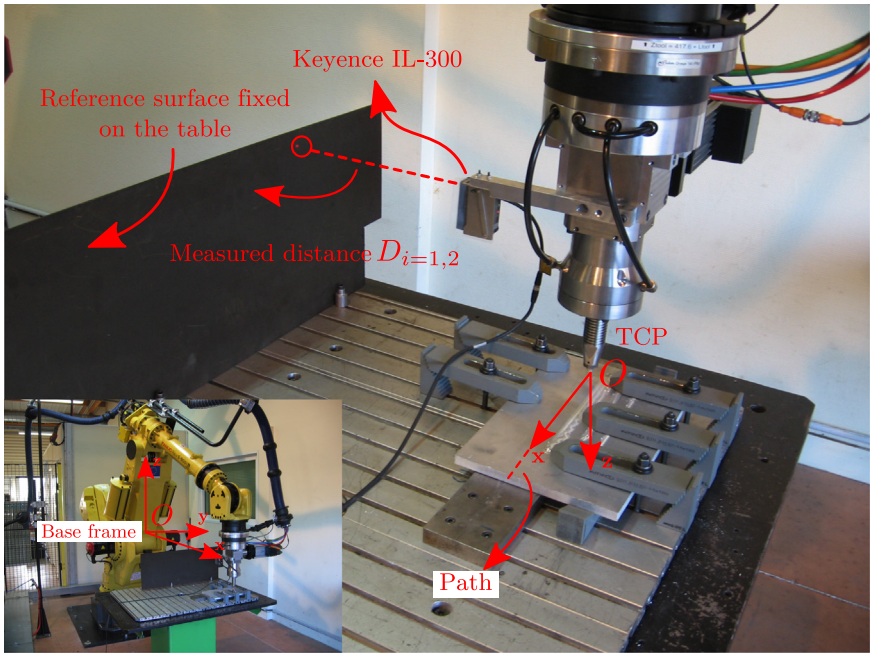

Fig. 15. Experimental set-up for the measurement of the real tool deviation Δy_r.

3.2.6. *Experimental validation of the elastostatic modeling*

The aim of this paper is based on many works dealing with the identification of robot elastostatic models [27,26,28]. However, in many cases, when experimental validations are performed on industrial robots, the corrected path is calculated by using an off-line post processor and the corrected path is injected into the robot controller [28]. However, this approach is not user-friendly and the industrial implementation can be difficult. Moreover, this method needs an environment model of FSW in order to predict accurately the forces along the welding path [28]. An another solution is using a dynamic elastic model in order to compensate the elastic deformations by a linear or non-linear feedback [33,17]. Outputs of this model are the motor torques. This approach is not viable in actual industrials robot as only the robot TCP pose can be controlled by the native language of the robot manufacturer. In this section, the identified elastostatic model is implemented in real-time in the industrial controller RJ3iB of the FANUC S900iB/400 robot. Therefore, the security and the conformity of the robot controller are preserved.

Fig. 14 shows the block diagram of the real time compensation embedding in the controller. The compensation of the lateral deviation is based on the force measurements performed by load cell sensor placed in the FSW end effector. Because of measurement noise, an average correction is done. The average is a percentage between 1 and 100% and leads to a smooth path correction, compatible with the FSW process. A lowest value of the average results in a fast correction. However, wobbling on the path can appear. A compromise between stability and correction speed has to be set up. In this paper, the percentage is fixed to 50%.

In order to verify the accuracy of the method, a laser distance sensor is used as shown in Fig. 15. The laser distance sensor is a Keyence IL-300 with an accuracy of 30 µm and a sample rate of 500 Hz. By convention, the **x** TCP axis is defined along the positive direction of the welding path. Therefore, the lateral tool deviation is along the **y** TCP axis. A weld of 250 mm is performed with a speed of 6 mm/s. Two welding paths are chosen at a distance of 1400 mm from the base frame. The first is done along the direction **y** + of the base frame and the second path is done along the direction **y** − of the base frame. Δy_m is the value of the lateral tool deviation calculated by the model, and Δy_r is the real value of the lateral tool deviation measured with the laser sensor. In order to calculate the real tool deviation Δy_r, the following procedure is carried out:

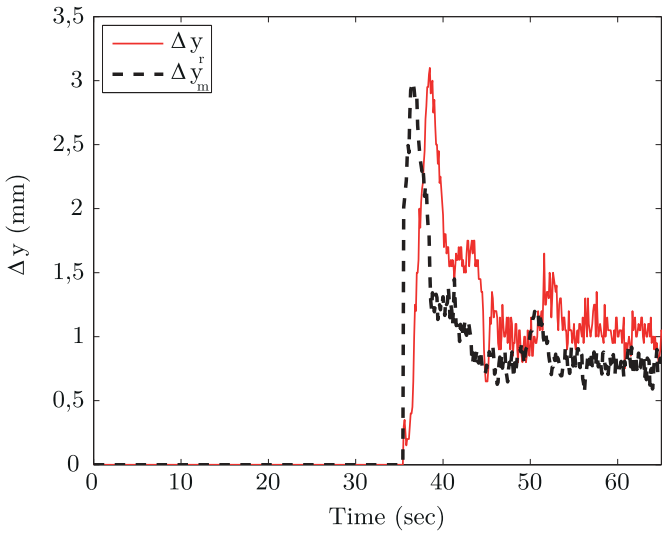

Fig. 16. Tool path direction **y** + .

- A first path is performed with no real time compensation. A distance D_1 is measured between the reference surface and the laser distance sensor.
- A second path is performed with real time compensation of Δy_m. A distance D_2 is measured between the reference surface and the laser distance sensor.
- The real tool deviation is done by $\Delta y_r = D_1 - D_2$.

Figs. 16 and 17 illustrate the evolution of the lateral tool deviation Δy_r and Δy_m on the two path.

As shown in Figs. 16 and 17, recordings of Δy_r and Δy_m are close. A delay can be observed between Δy_r and Δy_m due to the average calculation. Moreover, the direction of the weld path has an impact on the deviation, due to the direction of the welding force F_y. In fact, the welding force F_z has the same direction for the two paths,

however the force F_y is reversed between **y** + direction and **y** − direction. Fig. 18 shows the forces and the torques which are applied on the robot for the two different directions. The force F_z has the same direction for the two welding paths. The torques on axes 2 and 3 of the robot, and due to F_z, have the same direction for the two welding paths. On the other hand, between the two welding paths, the advancing side and the retreating side are reversed. Therefore, the direction of the force F_y is reversed. So the torques on axes 2, 3 and 5 of the robot, and due to F_y are also reversed. Consequently, the lateral tool deviation is lower when the path is performed along the **y** + direction.

Afterward, the real time compensation is applied in order to perform the butt weld which was done on the CNC machine in the first part of this paper. Fig. 19 shows the robot set-up. In this configuration, the FSW tool is at a distance of 1700 mm from the

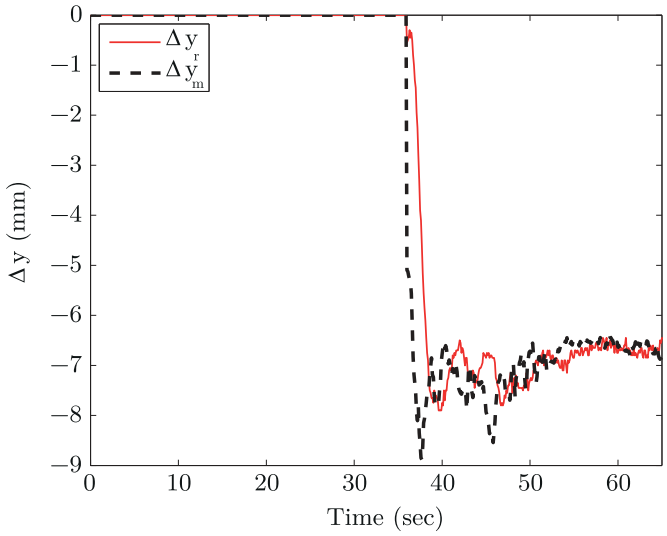

Fig. 17. Tool path direction **y** − .

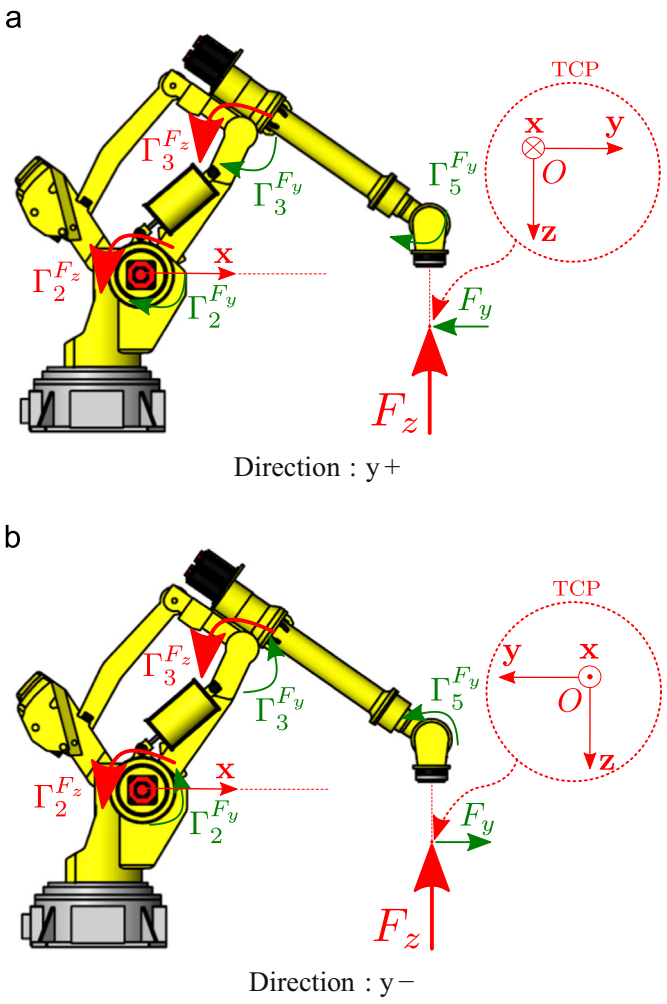

Fig. 18. Forces and torques which are applied on the robot. (a) Direction: **y** + . (b) Direction: **y** − .

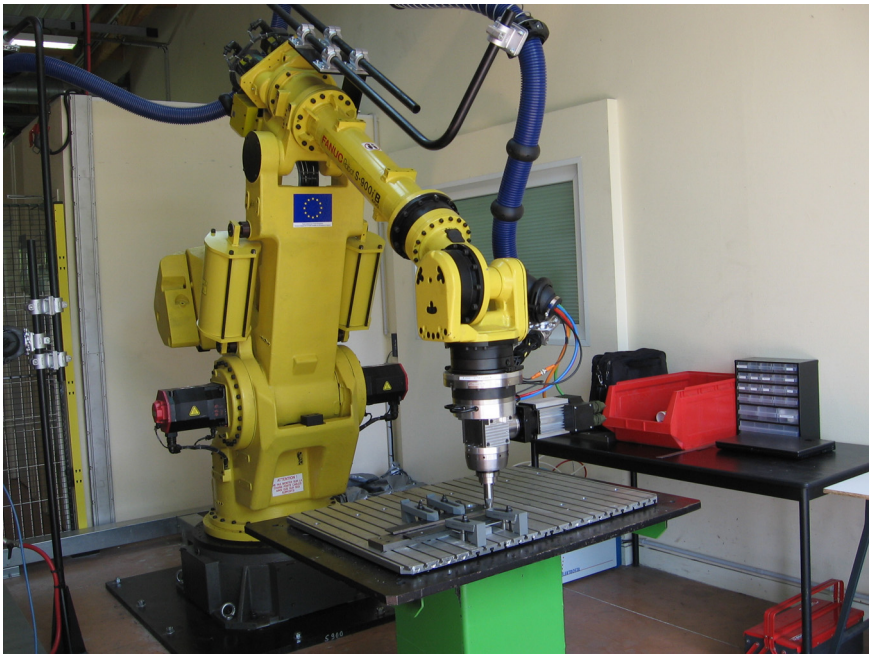

Fig. 19. Robot configuration for welding.

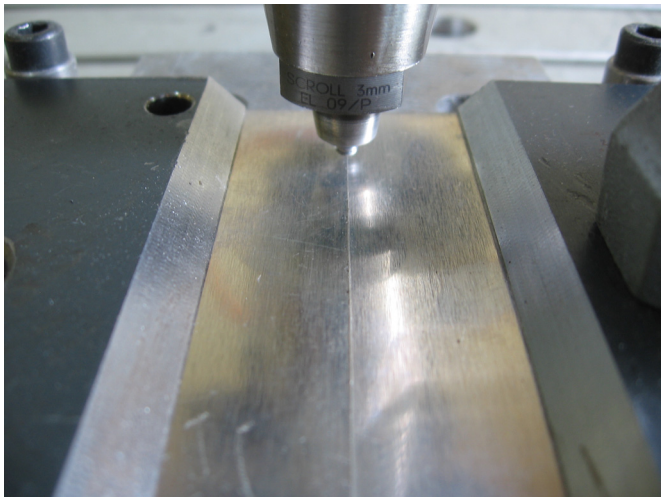

Fig. 20. Tool position before welding.

base frame of the robot. In this location, the robot stiffness is low, leading an important tool deviation.

Fig. 20 illustrated the pin position before welding. The programmed path is obtained by teaching the first and the last points of the weld joint. During no contact welding process, such as laser or arc welding, the robot tool is able to follow the programmed path. Only the robot repeatability affects the weld quality. In RFSW, important forces along all directions are applied on the tool and a deviation of several millimeters appears between the programmed path and the real path [17,24]. Therefore, the repeatability can be considered as second order error.

In our experiment, the lateral tool deviation is about 7 mm when the pin enters into the material. Considering the results of Section 3.1, a good weld quality cannot be achieved. In RFSW, three methods could be used to overcome this drawback. The first solution uses a fake target approach. The lateral tool deviation is measured on a RFSW sample without compensation. Then, the deviation is integrated manually in robot path. This method is a difficult task as the lateral tool deviation depends on different parameters (joint configuration, FSW process parameters and materials). This approach cannot be used in an industrial environment. The second solution uses a camera or laser sensor in order to track the weld seam path during welding. In an industrial perspective, this method can increase the flexibility. However, the cost of a seam tracking device, the aluminium reflexion and the lack of visibility in lap joint configuration are significant drawbacks [24]. The last solution uses specific algorithms developed in this paper. An elastostatic model of the robot done by Eq. (11) is used to estimate the deflection of the robot TCP.

Thereby, based on force measurements along the welding process, the corrected path is calculated in real time. Fig. 21 shows a weldment produced by the robot. The settling time is due to the average algorithm which is explained previously.

The compensation of the lateral tool deviation acts in combination with the force control algorithm. Fig. 22 shows the forces during FSW process, and Fig. 24 shows the different stages of the compensation. The objective is to respect a lateral tool deviation of $\pm$ 1 mm with the real-time compensation in order to get a good weld quality.

No failure is observed by optical microscopy on a bend sample obtained by RFSW with the real-time compensation. Moreover, metallographic examination does not reveal the presence of lack of penetration or kissing-bond defects. Based on three tensile tests, the meaning UTS obtained by using the robot is 200 MPa. Based on

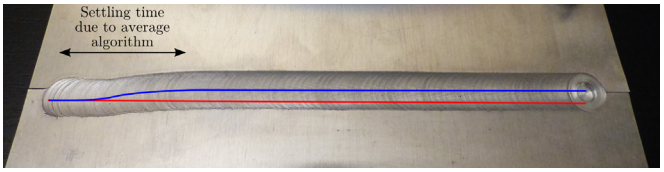

Fig. 21. Weldment produced on the FANUC S900iB/400: corrected path (blue); real path (red). (For interpretation of the references to color in this figure caption, the reader is referred to the web version of this paper.)

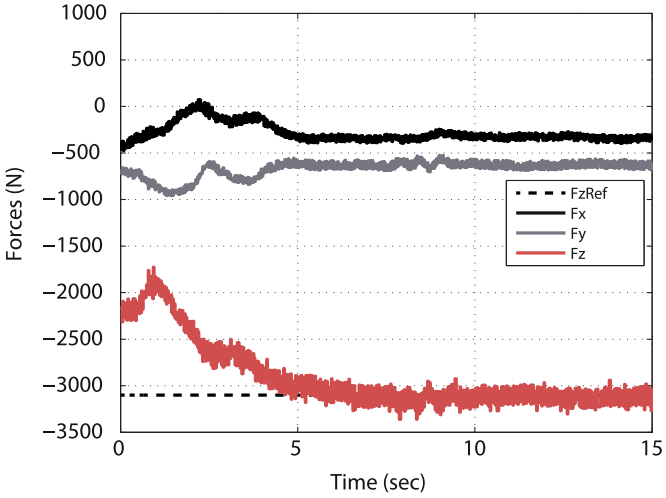

Fig. 22. Forces F_x, F_y and F_z during FSW process on the FANUC S900iB/400.

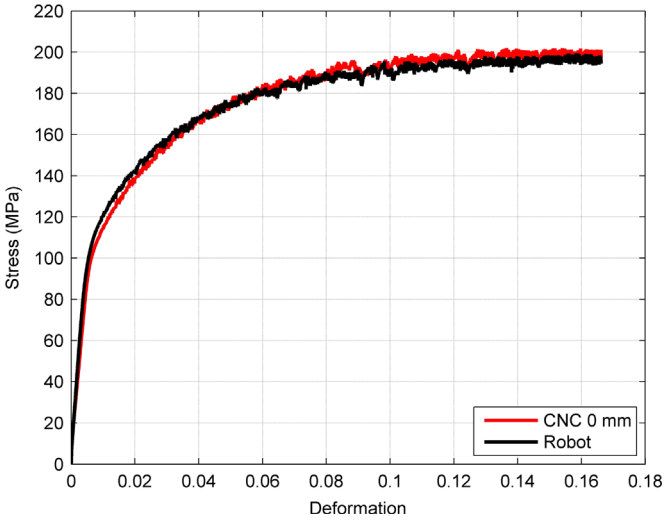

Fig. 23. Stress–strain curves of FSWed coupons made by CNC machine (pin offset of 0 mm) and RFSW.

these results, we can assume that the weld quality obtained using RFSW is equivalent that one performed on CNC system.

Fig. 23 shows the comparison between the stress–strain curves obtained with CNC system and the robot. Regarding UTS and elongation, the results are the same as those obtained with the CNC system.

4. Conclusion

In this paper, authors summarize the impact of pin axis position on FSWed quality, especially on the appearance of defects. The

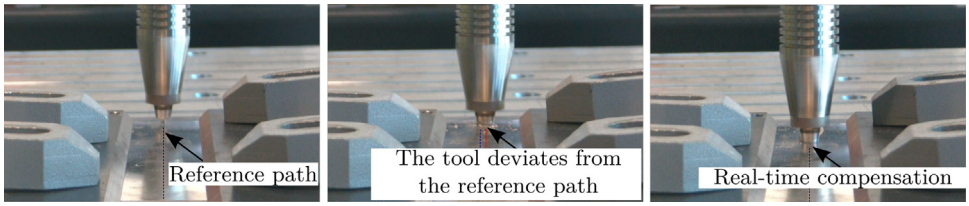

Fig. 24. The different stages of the real-time compensation of the lateral tool deviation

lack-of-penetration and kissing-bond defects are highlighted by metallurgical analysis, bending test and tensile properties. This experiment is carried out on a gantry-type CNC system and on an industrial robot. Firstly, FSW trials on CNC system show that the pin could be located into an offset of about -1.25 and 0.7 mm around the seam without impacting the weld quality. Secondly, in RFSW, important forces result in a lateral pin deviation of about 7 mm between the programmed path and the real path. Considering the results on CNC system, a good weld quality cannot be achieved. Therefore, the elastostatic model of an industrial robot is carried out by the classical identification technique and this model is embedded in the robot controller. Finally, the robot with the embedded algorithm can compensate the lateral pin deviation in real-time. This technique results in the same FSWed quality than a gantry-type CNC system.

Acknowledgments

The authors thank F. Gesvret and S. Evrat for technical support (FANUC Robotics France), R. Lemercier for CNC operating (BUGV), A. Anne for metallography (IM).

References

[1] P. Cavaliere, B. Nobile, W. Panella, et al., Mechanical and microstructural behaviour of 2024-7075 aluminium alloy sheets joined by friction stir welding, Int. J. Mach. Tools Manuf. 46 (6) (2006) 588–594.
[2] J.Q. Su, T.W. Nelson, R. Mishra, et al., Microstructural investigation of friction stir welded 7050-t651 aluminium, Acta Mater. 51 (3) (2003) 713–729.
[3] S.G. Russell, M. Tester, E. Nichols, et al., Static, fatigue and crack growth behavior of friction stir welded 7075-t6 and 2024-t3 aluminum alloys, in: Friction Stir Welding and Processing Conference, Indianapolis, USA, 2001.
[4] A. Murphy, M. Price, P. Wang, The integration of strength and process modeling of friction-stir-welded fuselage panels, in: 46th AIAA/ASME/ASCE/AHS/ASC Structures, Structural Dynamics, and Materials Conference, Austin, USA, 2005.
[5] J.Q. Su, T.W. Nelson, C.J. Sterling, Microstructure evolution during fsw/fsp of high strength aluminum alloys, Mater. Sci. Eng. A 405 (1–2) (2005) 277–286.
[6] B. Christner, J.M. Coury, S. Higgins, Development and testing of friction stir welding as a joining method for primary aircraft structure, in: 4th International Symposium on Friction Stir Welding, Park City, USA, 2003.
[7] L. Dubourg, R. Amargier, M. Jahazi, Relationship between fsw parameters, hardness and tensile properties of 7075-t6 and 2098-t851 similar butt welds, in: 7th International Friction Stir Welding Symposium, Awaji Island, Japan, 2008.
[8] L. Cederqvist, P. Reynolds, Factors affecting the properties of friction stir welded aluminum lap joints, Weld. J. 80 (12) (2006) 588–594.
[9] L. Dubourg, F.O. Gagnon, F. Nadeau, et al., Process window optimization for fsw of thin and thick sheet al alloys using statistical methods, in: 6th International Friction Stir Welding Symposium, Saint Sauveur, Canada, 2006.
[10] C.B. Smith, Robotic friction stir welding using a standard industrial robot, in: 2nd International Friction Stir Welding Symposium, Gothenburg, Sweden, 2000.
[11] A. Strombeck, C. Schilling, J. Santos, Robotic friction stir welding—tool technology and applications, in: 2nd International Friction Stir Welding Symposium, Gothenburg, Sweden, 2000.
[12] C.B. Smith, J.F. Hinrichs, W.A. Crusan, Robotic friction stir welding using a standard industrial robot, in: 4th International Friction Stir Welding Symposium, Salt Lake City, USA, 2003.
[13] M. Soron, I. Kalaykov, A robot prototype for friction stir welding, in: 4th International Friction Stir Welding Symposium, Orlando, USA, 2006.
[14] N. Mendes, P. Neto, M. Simao, et al., A novel friction stir welding robotic platform: welding polymeric materials, Int. J. Adv. Manuf. Technol. (2014) 1–10.
[15] G. Voellner, M.F. Zaeh, J. Silvanus, Influence of machine types on fsw seam qualities, in: 7th International Friction Stir Welding Symposium, Awaji, Japan, 2008.
[16] G. Voellner, M.F. Zaeh, J. Silvanus, et al., Robotic friction stir welding, in: Aerotech Congress & Exhibition, Los Angeles, USA, 2007.
[17] A. Bres, B. Monsarrat, L. Dubourg, et al., Simulation of robotic friction stir welding of aerospace components, Ind. Robot: Int. J. 37 (1) (2010) 36–50.
[18] M.F. Zaeh, G. Voellner, Three-dimensional friction stir welding using a high payload industrial robot, Product. Eng. 4 (2–3) (2010) 127–133.
[19] J. Wang, H. Zhang, T. Fuhlbrigge, Improving machining accuracy with robot deformation, in: IEEE International Conference on Intelligent Robots and Systems, St. Louis, USA, 2009.
[20] J. De Backer, M. Soron, T. Ilar, et al., Friction stir welding with robot for light weight vehicle design, in: 8th International Friction Stir Welding Symposium, Timmendorfer Strand, Germany, 2010.
[21] M. Soron, J. De Backer, A.K. Christiansson, et al., A local model for online path corrections in friction stir welding, in: Friction Stir Welding and Processing Conference, Lille, France, 2010.
[22] O. Marcotte, L. Vanden-Abeele, 2d and 3d friction stir welding with articulated robot arm, in: 8th International Friction Stir Welding Symposium, Timmendorfer Strand, Germany, 2010.
[23] S. Zimmer, L. Langlois, J. Laye, et al., Experimental investigation of the influence of the fsw plunge processing parameters on the maximum generated force and torque, Int. J. Adv. Manuf. Technol. 47 (1-4) (2010) 201–215.
[24] J. De Backer, A.K. Christiansson, J. Oqueka, et al., Investigation of path compensation methods for robotic friction stir welding, Ind. Robot: Int. J. 39 (6) (2012) 601–608.
[25] W.R. Longhurst, A.M. Strauss, G.E. Cook, et al., Investigation of force-controlled friction stir welding for manufacturing and automation, Proc. Inst. Mech. Eng. Part B: J. Eng. Manuf. 224 (6) (2010) 937–949.
[26] G. Alici, B. Shirinzadeh, Enhanced stiffness modeling, identification and characterization for robot manipulators, IEEE Trans. Robot. 21 (4) (2005) 554–564.
[27] C. Dumas, S.K. Caro, S. Garnier, et al., Joint stiffness identification of six-revolute industrial serial robots, Robot. Comput.-Integr. Manuf. 39 (4) (2011) 881–888.
[28] J. Belchior, M. Guillo, E. Courteille, et al., Off-line compensation of the tool path deviations on robotic machining: application to incremental sheet forming, Robot. Comput.-Integr. Manuf. 29 (2013) 58–69.
[29] P.L. Threadgill, A.J. Leonard, H.R. Shercliff, et al., Friction stir welding of aluminium alloys, Int. Mater. Rev. 54 (2) (2009) 49–93.
[30] C. Mandache, D. Levesque, L. Dubourg, et al., Non-destructive detection of lack of penetration defects in friction stir welds, Sci. Technol. Weld. Join. 17 (4) (2012) 295–303.
[31] W. Khalil, E. Dombre, Modeling, Identification and Controls of Robots, 2nd ed., Hermes Penton Ltd, 2002.
[32] S.F. Chen, The 6×6 stiffness formulation and transformation of serial manipulators via the cct theory, in: IEEE International Conference on Robotics & Automation, Taiwan, 2003.
[33] M.W. Spong, K. Khorasani, P.V. Kokotovic, An integral manifold approach to the feedback control of flexible joint robots, IEEE J. Robot. Autom. 3 (4) (1987) 291–300.